Composites Part B 180 (2020) 107564

Contents lists available at ScienceDirect

Composites Part B

journal homepage: www.elsevier.com/locate/compositesb

Study the safeguarding performance of shear thickening gel by the mechanoluminescence method

Shuaishuai Zhang [a], Sheng Wang [a], Tao Hu [a], Shouhu Xuan [a,**], Han Jiang [b], Xinglong Gong [a,*]

[a] CAS Key Laboratory of Mechanical Behavior and Design of Materials, Department of Modern Mechanics, University of Science and Technology of China (USTC), Hefei, Anhui, 230027, PR China

[b] Applied Mechanics and Structure Safety Key Laboratory of Sichuan Province, School of Mechanics and Engineering, Southwest Jiaotong University, PR China

ARTICLE INFO

Keywords:
Shear thickening
Safeguarding
Mechanoluminescence
Energy map
Phase change
Crack

ABSTRACT

This work reports the potential of a full-field, simple-setup and user-interactive method to study the safeguarding property of shear thickening gel (STG) by converting the invisible force/energy information to visible mechanoluminescence. Both the instantaneous intensity and force signals under impact prove the phase change of STG from viscous liquid state to rubbery state. The illumination images, presenting the energy maps, directly visualize the remarkably expanded impact area and phase change induced energy absorption, promoting the understanding of safeguarding mechanisms. The shear thickening property and viscoelastic deformation of STG significantly expand the impact area by almost 5 times, spreading and dissipating force/energy significantly. Moreover, the phase change accompanied by cracks is observed clearly, which is demonstrated to be beneficial to the energy absorption and contributes to the further enlargement of the impact area.

1. Introduction

Shear thickening (ST) materials [1,2], whose viscosity or modulus increases dramatically with the strain rate, have drawn worldwide attention due to the perspective in the safeguarding area [3–5]. For real-world applications, the force/energy absorption performance of ST based devices is the key focus of the researchers and various test methods have been adopted in studying the related phenomenon and mechanisms. Employing traditional dynamic methods, shear thickening fluid (STF) based devices exhibited outstanding energy absorption performance in ballistic [6,7] and impact [8,9] tests. For example, by packaging the viscous STF into polyurea shells, the STF capsules exhibited enhanced anti-impact performance and reliable practicability [10,11]. Avoiding the sedimentation disadvantage of STF, shear thickening gel (STG), whose modulus boosts 3–4 orders of magnitude with the increase of shear frequency, has drawn more and more attention [12]. The split Hopkinson bar tests proved that the energy absorption characteristic of STG was responded for the rate-dependent phase change, from viscous liquid state to rubbery state and glassy state [13]. With help of the acceleration sensor and force sensor, STG based nanodevices were proven to disperse impact by expanding the impact area with declining the impact force from 1687.37 N to 566.40 N [14]. Unfortunately, those methods could only provide spatially accumulated information of the detection area and thus were inherently limited in full-field stress/energy analysis. Recently, by introducing high-speed ultrasound method, Han imaged the three-dimension jamming by shear, providing direct proof of stress dispersion under impact [15]. However, this method was an indirect visualization and desired expensive high-speed ultrasound emission source and detector. Therefore, the development of a method for full-field, simple-setup and human-readable force/energy absorption monitoring is appealing for both the academic research and safeguarding applications of ST materials.

Mechanoluminescence is the emission of cold light due to mechanical excitation sources, such as compression and impact. A great number of materials have already been identified to be mechanoluminescent [16,17] and excellent research works have been done to study the related behaviors [18] and underlying mechanisms [19,20]. For example, a mechanoluminescence device, embedding ZnS:Mn and ZnS:Cu particles in polydimethylsiloxane (PDMS), emitted significant brightness and a range of tunable white colors upon gas flow [21]. Avoiding the requirement of an artificial photon- or electron-excitation

* Corresponding author.
** Corresponding author.
E-mail addresses: xuansh@ustc.edu.cn (S. Xuan), gongxl@ustc.edu.cn (X. Gong).

https://doi.org/10.1016/j.compositesb.2019.107564
Received 15 August 2019; Received in revised form 26 October 2019; Accepted 29 October 2019
Available online 1 November 2019

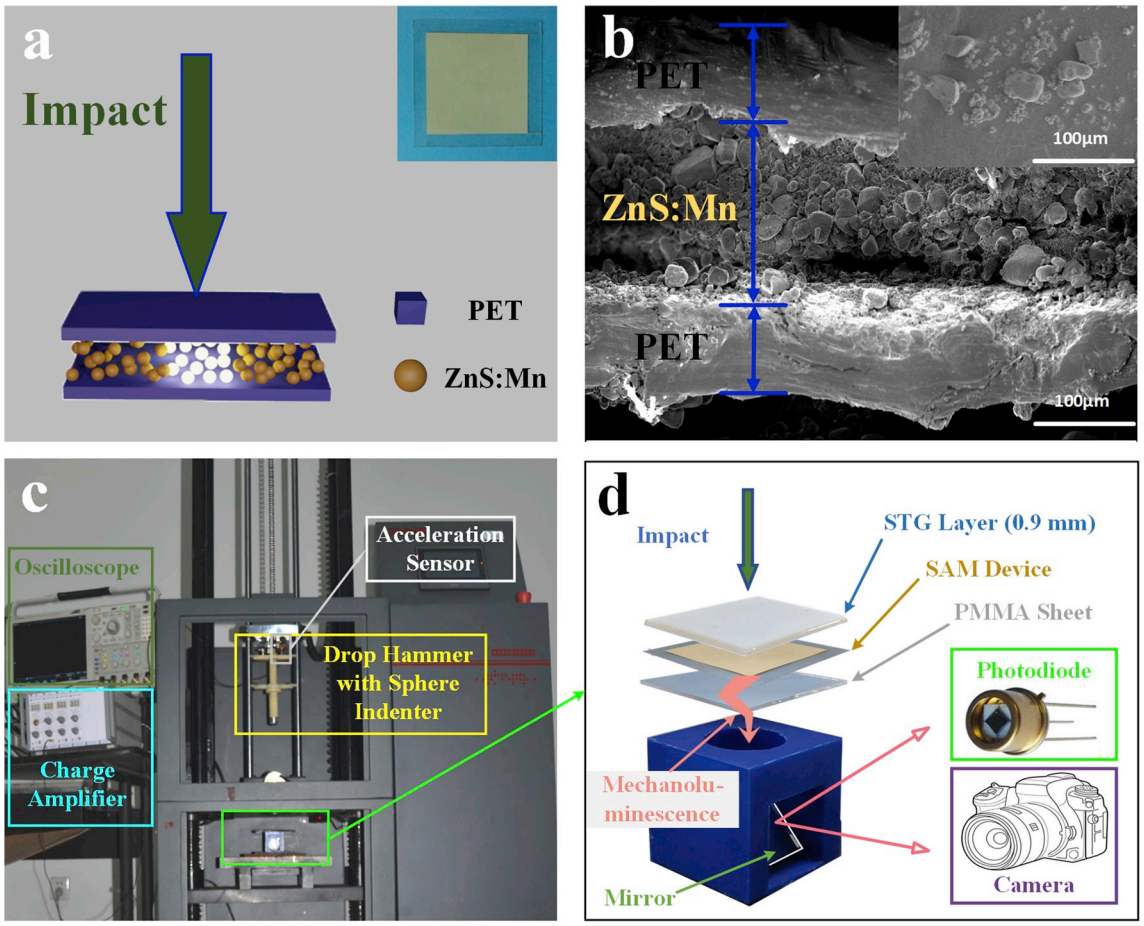

Fig. 1. The schematic diagram (a) and picture (inset) of the SAM device. The SEM images of the SAM device (b) and ZnS:Mn particles (inset). The experimental setup of impact tests (c). The setup of illumination acquisition system (d).

source, this device was further applied in energy harvesting and environmentally friendly light resources based on wind motion. By doping SiO_2 nanoparticles and ZnS:Mn microparticles into soft PDMS, a skin-driven device exhibited human-readable responses to lips corner, canthus, and cheek muscle movements, paving a way for human social interactions [22]. These works provided solid evidence for the promising potential of mechanoluminescence materials in user-interactive sensing area [23]. Unfortunately, most studies utilized the mechanoluminescence property in a simple way ignoring the fundamental physical information. Conventionally, the emitted mechanoluminescence intensity carries a twofold meaning, namely the instantaneous intensity and the accumulated intensity. The former, usually captured by photodiode, is directly related to stress [24,25] and widely used in dynamic pressure sensing [26–28] and energy harvesting [29]. The latter, commonly recorded with a long exposure camera, is the integration of instantaneous intensity with time and it is proportional to the applied energy [30]. Relying on the instantaneous visual response to stress, Wang applied ZnS:Mn powders in a user-interactive e-skin, allowing the dynamic pressure profile to be both spatially mapped and visually seen [27]. Similarly, a real-time pressure mapping device successfully tracked the dynamic signing process with a time response of 10 ms and spatial-resolution of less than 100 μm (254 dpi) [31]. Kersemans reconstructed the three-dimension ultrasonic spatial power field using the accumulated illumination images emitted from $SrAl_2O_4$:Eu phosphor [32]. Thus, by transforming invisible stress or energy information of samples into visible luminesce signals, the mechanoluminescence method is effective in the monitoring of stress or energy with the merits of easy identification, full-field, and real-time response. Therefore, the method based on the instantaneous and accumulated mechanoluminescence may pave a way in the safeguarding performance study of STG by the direct visualization of stress and energy.

Based on the mechanoluminescence of ZnS:Mn particles, the force/energy absorption behavior of shear thickening gel (STG) is studied and the key factors for safeguarding performance are discussed. STG exhibits a unique rate-dependent property with the storage modulus rising from 100 Pa to 0.32 MPa with the increase of shear frequency. Upon impact, the STG layer with a thickness of 0.9 mm buffers the impact force by 24.9%, presenting impressive protective performance. Simultaneously, the phase change of STG is evidenced in both the force and instantaneous intensity signals. The integrated intensity is proportional to applied energy with a factor of 112 nJ/J and 1.36 a.u./J, exhibiting a good correlation with the theory. Besides, the energy absorption at 0.735 J impact energy is demonstrated to reach 0.51 J. The visualization of energy density maps matches the theory well and provides more details of physical foundations, promoting the understanding of the safeguarding mechanisms. The significant enlargement of the impact area, due to the viscoelastic deformation and shear thickening behavior of STG, absorbs impact force and energy forcefully. High strain rate induced phase change and cracks contribute to the energy absorption and further enlarge the impact area.

2. Experiment section

2.1. Materials

Ethanol and boric acid were purchased from Sinopharm Chemical Reagent Co. Ltd., Shanghai, China. Hydroxyl silicone oil (PDMS, 500 mm^2/s, AR degree, from Jining Huakai Resin Co., Ltd) was used to

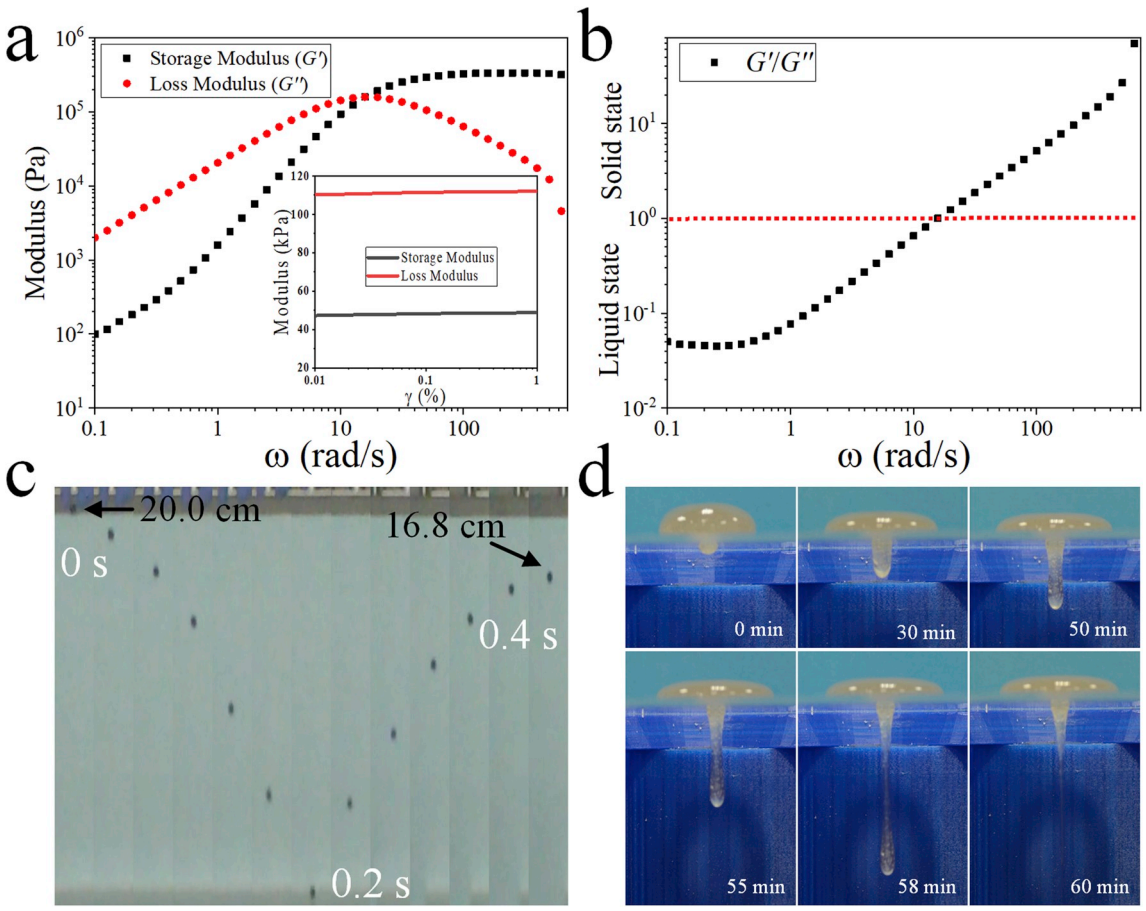

Fig. 2. The rheological property (a) and the physical state of STG (b). The results of dynamic rebound (c) and static creep (d) tests.

prepare shear thickening gel (STG). Polyethylene terephthalate (PET) films with a thickness of 0.1 mm were commercially available products. ZnS:Mn powders were purchased from Shanghai Koray Technology Co. Ltd., Shanghai, China.

2.2. Experiments

By thoroughly stirring, 5 g boric acid and 100 ml hydroxyl silicone oil were mixed evenly in a ceramic dish. Then, the mixture was heated at 180 °C for 1.5 h and was stirred every 15 min to ensure the homogeneous reaction. The mixture formed cross-linked, sticky and viscous gel during the heating process. After cooling to room temperature, the shear thickening gel (STG) was obtained [33]. During the fabrication process, the hydroxyl silicone oil was successfully cross-linked by chemical Si–O–B bonds with the introduction of boric acid. More importantly, the physical crosslinks between boron and oxygen atoms from different molecules were incorporated, which resulted in the rate-dependent property of STG directly [34].

ZnS:Mn powders were first ultrasonically dispersed in ethanol, then was transferred on a thin polyethylene terephthalate (PET) film with a size of 8 cm × 8 cm immediately. The film edges were enclosed with double-sided tapes. After gently smoothing and shaving, a flat layer of uniform ZnS:Mn particles were deposited on the film. As the ethanol was volatilized totally, the film was covered by another piece of PET film and was packaged with double-sided tapes. To obtain a better package, the stress-activated- mechanoluminescence device (SAM, Fig. 1a inset) was compacted tightly under 20 kg weight for 2 days and thus exhibited good uniformity.

2.3. Characterization

The morphology of ZnS:Mn particles and the SAM device were characterized by field emission scanning electron microscopy (FE-SEM, XL30 ESEM). The rheological property of STG was tested by using a commercial rheometer (Physica MCR302, Anton Paar Co., Austria). The samples, molded into a cylinder shape with a thickness of 1 mm and diameter of 20 mm, were tested with a parallel plate (diameter: 20 mm). At the frequency sweep tests, the shear frequency increased exponentially from 0.1 rad/s to 628 rad/s and the strain was set at 0.1%. At the strain sweep tests, the shear frequency was set at 6.28 rad/s and the strain increased exponentially from 0.01% to 1%.

To investigate the safeguarding performance of STG by using the SAM device, impact tests (Fig. 1c) were carried out with the drop tower machine (ZCJ1302-A, MTS System Co., America). The drop hammer (mass: 0.25 kg) with a sphere indenter (diameter: 20 mm) was released from different heights and its falling was limited within two paralleling vertical rods. An acceleration sensor was equipped on the drop hammer to capture the acceleration signals during the impact process. Then, the signals passed through the signal-amplifier and finally were recorded in the oscilloscope. The acquisition of mechanoluminescence was carried out on a home-built system (Fig. 1d). The SAM device was placed on a polymethyl methacrylate (PMMA) sheet with a thickness of 5 mm. The PMMA sheet was fixed supported on a polylactide frame (diameter: 30 mm). A flat mirror, right underneath the transparent PMMA sheet at a 45° angle, was applied to change the mechanoluminescence direction and assist the record of emission. The above device was fixed right under the drop hammer. Due to the plastic nature of STG at low strain rate, it could be easily molded to a thin layer with a thickness of 0.9 mm in a metal mold by simply using a roller. As the drop hammer pounded on the

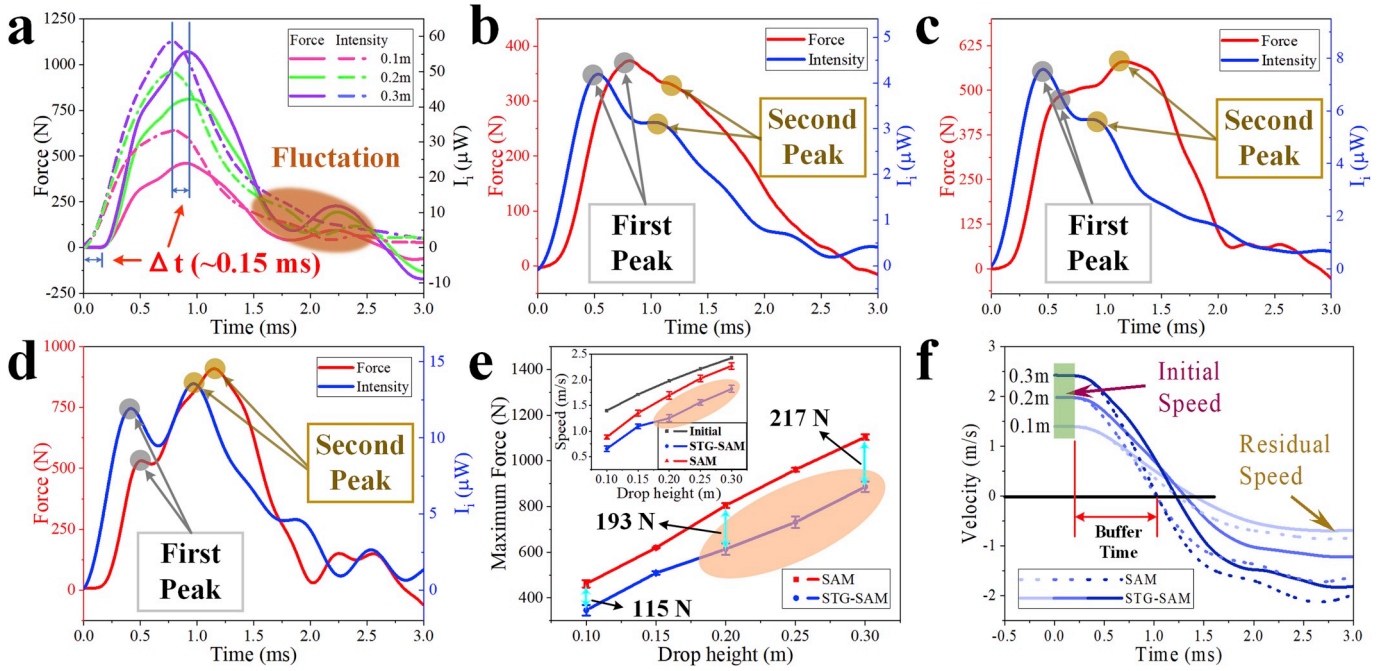

Fig. 3. The force and instantaneous intensity (I_i, captured by photodiode) responses under impact. The force-time and I_i-time relations as the drop hammer pounded on the SAM device from different height (a). The force-time and I_i-time relations as the drop hammer pounded on the STG-SAM device from 0.1 m (b), 0.2 m (c) and 0.3 m (d). The maximum force (e), initial speed and residual speed (inset) versus drop height. The speed of drop hammer during the impact process (f).

SAM device or STG layer covered SAM (STG-SAM) device, ZnS:Mn particles could illuminate visible orange light. A photodiode (Beijing Lightsensing Technologies Ltd, type: LSSPD) was applied to record the space-integrated instantaneous intensity (I_i). A camera (Nikon digital camera, type: D7000) was set at 6 s exposure mode to capture the illumination images. The time-accumulated illumination intensity (I_a) distribution and impact area were extracted from the above images by using Matlab 2018b software. The impact tests were all conducted in a dark room to decline the noise as much as possible.

3. Results and discussion

3.1. Structure and morphology of SAM device

Mechanoluminescent ZnS:Mn powders, sandwiched between two PET films, could illuminate strong light under appropriate external stimulus such as impact (Fig. 1a). Thanks to the outstanding toughness, PET films with a thickness of about 100 μm served as cushion layers to protect ZnS:Mn powders from concentrated stress. Besides, its high transparency benefited the transmission of the illuminated orange light. The scanning electron microscopy (SEM) image confirmed the compact layered state of ZnS:Mn particles and PET films (Fig. 1b). The size of ZnS:Mn particles dispersed in a wide range between 0.5 and 40 μm (Fig. 1b inset). Except some large particles, most particles were small (0.5–10 μm). Besides, the statistic size results of ZnS:Mn particles before and after sandwiched between PET layers were almost identical (Fig. S1). The thickness of ZnS:Mn layer exhibited good uniformity (about 190 ± 15 μm), enable it to be reliable for practical applications.

3.2. Rheological property of STG

The impressive energy absorption capability of STG is primarily attributed to its unique rate-dependent mechanical property (Fig. 2a). When the shear frequency is 0.1 rad/s, the storage modulus (G') is 100 Pa, exhibiting a soft and plastic property. Once the frequency reaches 628 rad/s, its storage modulus rises to 0.32 MPa, which is 3 orders higher than initial G'. The rate-dependent mechanical behavior of STG is mainly attributed to the physical crosslinks between boron and oxygen atoms from different molecules. Different from those permanently connected chemical bonds, the physical crosslinks can undergo rate-dependent breaking and reattaching processes [35]. At low strain rate, these dynamic crosslinks break and reattach freely and carry almost no loads. Therefore, STG is at viscous liquid state and deforms easily. At high strain rate, there is no enough time for the attached dynamic crosslinks to break. The attached dynamic crosslinks behave like permanent chemical bonds and restrict the deformation severely [36]. Thus, STG transforms into rubbery state, exhibiting a much larger modulus. The loss modulus (G'') at first increases with the frequency and then decreases at 15.8 rad/s with a peak of 0.16 MPa. In addition, as the frequency is kept at 6.28 rad/s, the storage and loss modulus are almost irrelevant with the shear strain in a range of 0.01%–1% (Fig. 2a inset). The ratio of storage modulus to loss modulus is an important factor to evaluate the material state (Fig. 2b). STG is soft and plastic (liquid-like state) at low frequency and becomes tough as frequency increases. As the frequency is larger than 15.8 rad/s, storage modulus exceeds loss modulus, presenting a solid-like property.

To demonstrate the rate-dependent property of STG in a visible way, the dynamic rebound test (high strain rate) and static creep test (low strain rate) were carried out. Normally, STG was transparent and colorless. For clear observation, minor blue ink was doped in STG. As the STG ball with a diameter of about 5 mm was released from 20 cm, it collided upon the bottom plate at 0.2 s and bounced back to almost 80% the initial height at 0.4 s (Fig. 2c). As STG was placed upon a plate where a hole was drilled, it collapsed gradually and flowed out from the hole within 1 h (Fig. 2d). In summary, STG behaved an elastic property at high strain rate, while it was soft and flowed like liquid at low strain rate.

3.3. Force and I_i responses of SAM and STG-SAM devices under impact

Due to the unique rate-dependent property of STG, it could buffer force under impact and the dynamic process was directly captured by acceleration sensor and photodiode (Fig. 3). Applying Newton's second law of motion, the force signals were obtained by multiplying the

acceleration data by the mass of drop hammer. Apparently, the force signals delayed about 0.15 ms compared with I_i signals, which was mainly induced by the propagation of stress wave from the indenter tip to the acceleration sensor. As the drop hammer pounded on the SAM device directly from 0.1 m (Fig. 3a), force increased linearly at first. Simultaneously, the applied impact energy was transferred to the ZnS: Mn particles which illuminated strong orange light and I_i of the impact zone over time could be expressed as:

$$I_{i-r}(t) \propto F(t) \tag{1}$$

where $I_{i\text{-}r}$ is the I_i at the rise stage, t is the time and F is the applied force. Correspondingly, I_i increased synchronously with the rise of force, consistent with the theory. Then, the force reached a peak value of 460 N at nearly 0.92 ms. Simultaneously, I_i also attained maximum value (33.3 μW). After that, the force decreased gradually. At this process, the I_i decayed exponentially with time as:

$$I_{i-d} = I_0 \exp[-\varnothing (t - t_0)] \tag{2}$$

where $I_{i\text{-}d}$ is the I_i at the decay stage, I_0 is the peak I_i at $t = t_0$ and $\varnothing$ is the decay coefficient which could be determined by experiments. Here, $\varnothing$ was about 1805 s^{-1} (Fig. S2). Notably, the force signal rose moderately again at about 2 ms, which was probably caused by the mismatch of deformation between the drop hammer and the SAM device. A corresponding fluctuation of I_i also occurred at the same time. Reasonably, the drop height behaved a positive influence on force and I_i signals. For example, raising drop height from 0.1 m to 0.2 m and 0.3 m, the peak force increased from 460 N to 811 N and 1070 N, respectively. Similarly, the peak I_i was also enhanced from 33.3 μW to 46.6 μW and 58.9 μW, exhibiting a high force sensitivity. Traditionally, the force/stress was measured by electric resistance strain gauges [37,38] and piezoelectric sensors [39–42], which required complex electric circuits [43]. Here, this mechanoluminescence method, enjoying the advantages of simple-setup and real-time, also demonstrated great potential in the force sensing area.

As the drop hammer pounded on the STG-SAM device from 0.1 m, the force at first increased linearly and then decreased gradually (Fig. 3b). However, an immediate lower second peak (brown circles) was observed following the first peak (gray circles). The double peaks also appeared as the drop height rose to 0.2 m and 0.3 m (Fig. 3c–d). At low strain rate, STG was in viscous liquid state and unloaded immediately after the yield point (first peak). However, the expanded contact area during the impact process caused the feeble second peak. As the drop height was lifted to 0.2 m and 0.3 m, STG transformed from viscous liquid state to rubbery state due to the high strain rate [13]. A hardening process occurred after the yield point (first peak) and resulted in the second rise of force (second peak). Interestingly, the first peak force, presenting the yield point of STG, increased from 373 N to 482 N and 531 N with the drop height, demonstrating a typical shear thickening property. The increase of second peak force was much larger, which rose significantly from 330 N to 580 N and 909 N. Additionally, the time of first force peak shifted forward with the drop height gradually from 0.80 ms to 0.60 ms and 0.51 ms, which resulted from the increase of impact speed. However, the time of the second force peak kept nearly constant (~1.25 ms), indicating a longer hardening duration at a higher

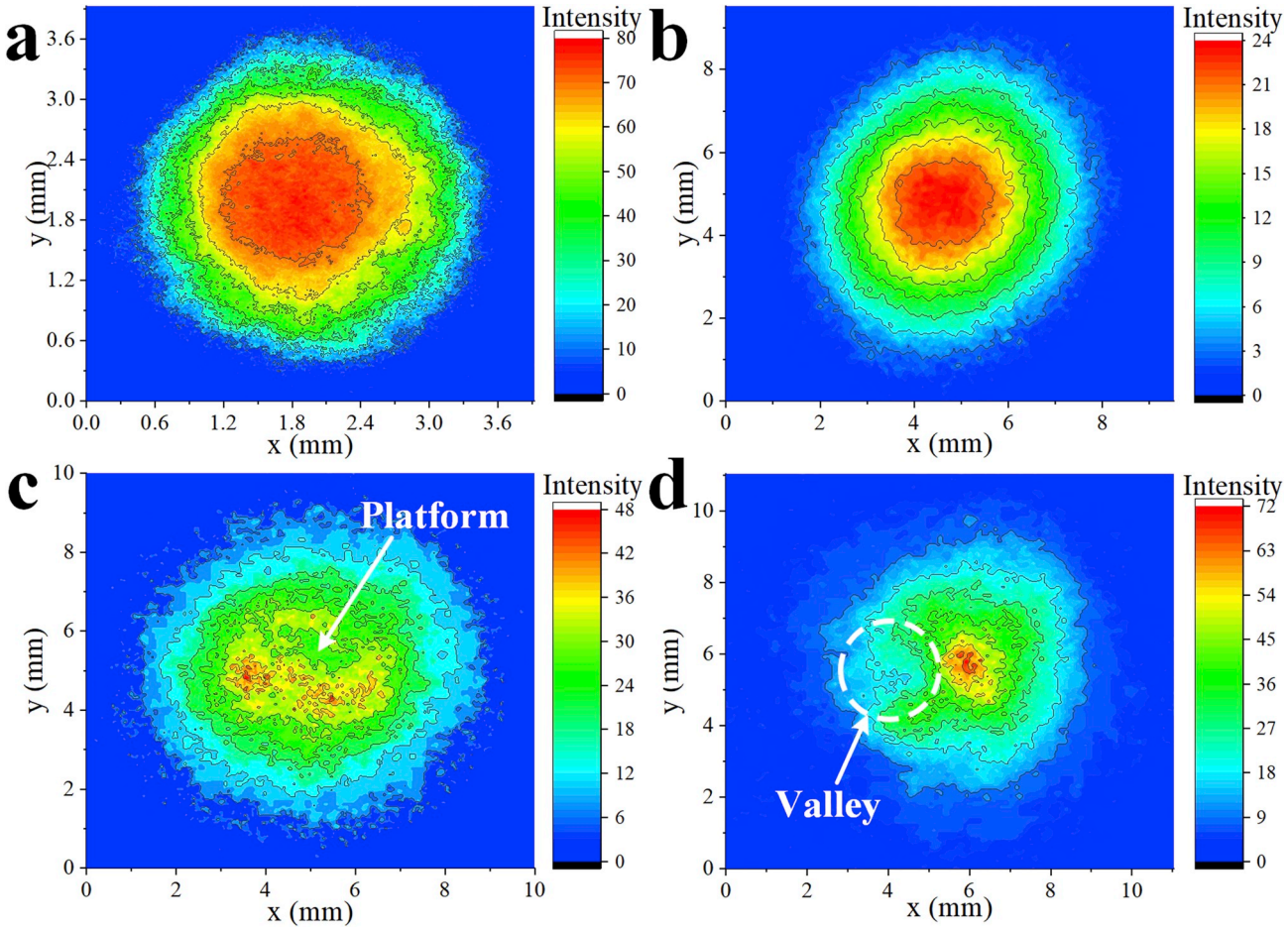

Fig. 4. The time-accumulated intensity (I_a) distribution over space which were extracted from the illumination images captured by a camera. The spatial I_a distribution as the drop hammer pounded on the SAM device from 0.1 m (a). The spatial I_a distribution as the drop hammer pounded on STG-SAM device from 0.1 m (b), 0.2 m (c) and 0.3 m (d).

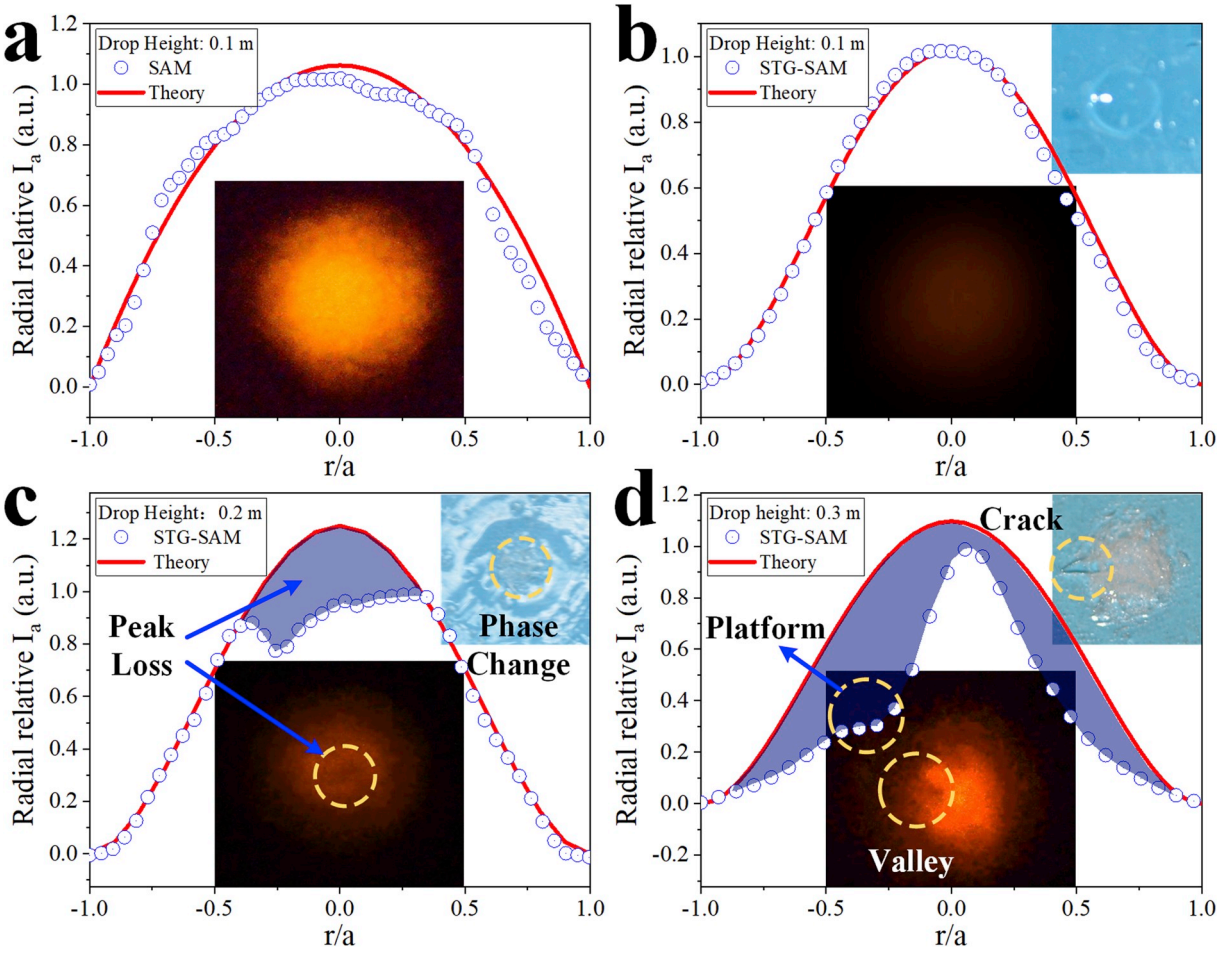

Fig. 5. The comparison of radial relative I_a distribution with theory curve and the illumination image (middle inset) as the drop hammer pounded on the SAM device from 0.1 m (a). The comparison of radial relative I_a distribution with theory curve, the illumination image (middle inset) and image of STG layer after impact (upper right inset) as the drop hammer pounded on STG-SAM device from 0.1 m (b), 0.2 m (c) and 0.3 m (d), respectively. In the horizontal axis, a is the impact zone radius and r is the local radius.

strain rate. Thus, the dynamic strength of STG was enhanced significantly by the increase of strain rate.

I_i demonstrated a similar trend according to equations (1) and (2). The drop height behaved a positive influence on both peaks of I_i. As the drop height rose from 0.1 m to 0.2 m, the first peak I_i increased from 4.20 μW to 7.52 μW and the second peak I_i increased from 3.15 μW to 5.51 μW. Differently, at 0.3 m drop height, the second peak I_i rose much higher and reached 13.5 μW, exceeding the first peak I_i (12.1 μW). This was mainly attributed to the longer hardening time of STG at high strain rate. Besides, fluctuations also appeared in the force and I_i signals at the decay process.

The safeguarding performance of STG was evaluated by measuring the averaged maximum force of five tests (Fig. 3e). Notably, the maximum force increased almost linearly with the drop height. STG demonstrated outstanding anti-impact behavior by buffering impact force. For example, the maximum force decreased from 461 N to 346 N (by 24.9%) at 0.1 m drop height owing to shear thickening behavior of STG. As the drop hammer rose to 0.2 m and 0.3 m, the maximum force was declined by STG from 804 N and 1103 N to 613 N and 886 N, respectively. Notably, the maximum force disparity increased with the drop height from 115 N to 193 N and 217 N. At low strain rate, the viscoelastic deformation of STG dissipated the impact force. At high strain rate, the phase change of STG from viscous liquid state to rubbery state further absorbed the impact force, thus enlarged the disparity values.

By integrating the acceleration signals, the speed-time relations of drop hammer during the impact process were obtained (Fig. 3f). The initial speed values were related to the drop height directly as

$$v = \sqrt{2gh} \tag{3}$$

where v is the speed of drop hammer, g is the gravity and h is the drop height. As the drop hammer pounded on the SAM device, the speed of drop hammer decreased from initial values to zero quickly and the duration was the buffer time. Then the speed increased inversely as the drop hammer bounced back. Increasing the drop height from 0.1 m to 0.3 m reduced the buffer time from 1.09 ms to 0.88 ms owing to the growing impact force. As the drop height was kept at 0.3 m, the equipment of the STG layer lengthened the buffer time from 0.88 ms to 1.07 ms (by 21.6%). The enlargement of buffer time also contributed to the dissipation of impact force. The speed of bouncing back was named as residual speed (Fig. 3e inset). The initial speed increased with drop height following a power law of 0.5 (black line). The residual speed of SAM sample (red line) was smaller due to structure friction and damping. As the STG layer was equipped, the residual speed (blue line) was reduced apparently, resulting from the energy absorption characteristic of STG. Thanks to the STG phase change induced energy absorption at high strain rate, the increase of residual speed was blocked as drop height surpassed 0.2 m (orange ellipse in Fig. 3e), similar to the force signals.

The total I_i (Fig. S3a) was obtained by integrating the I_i as

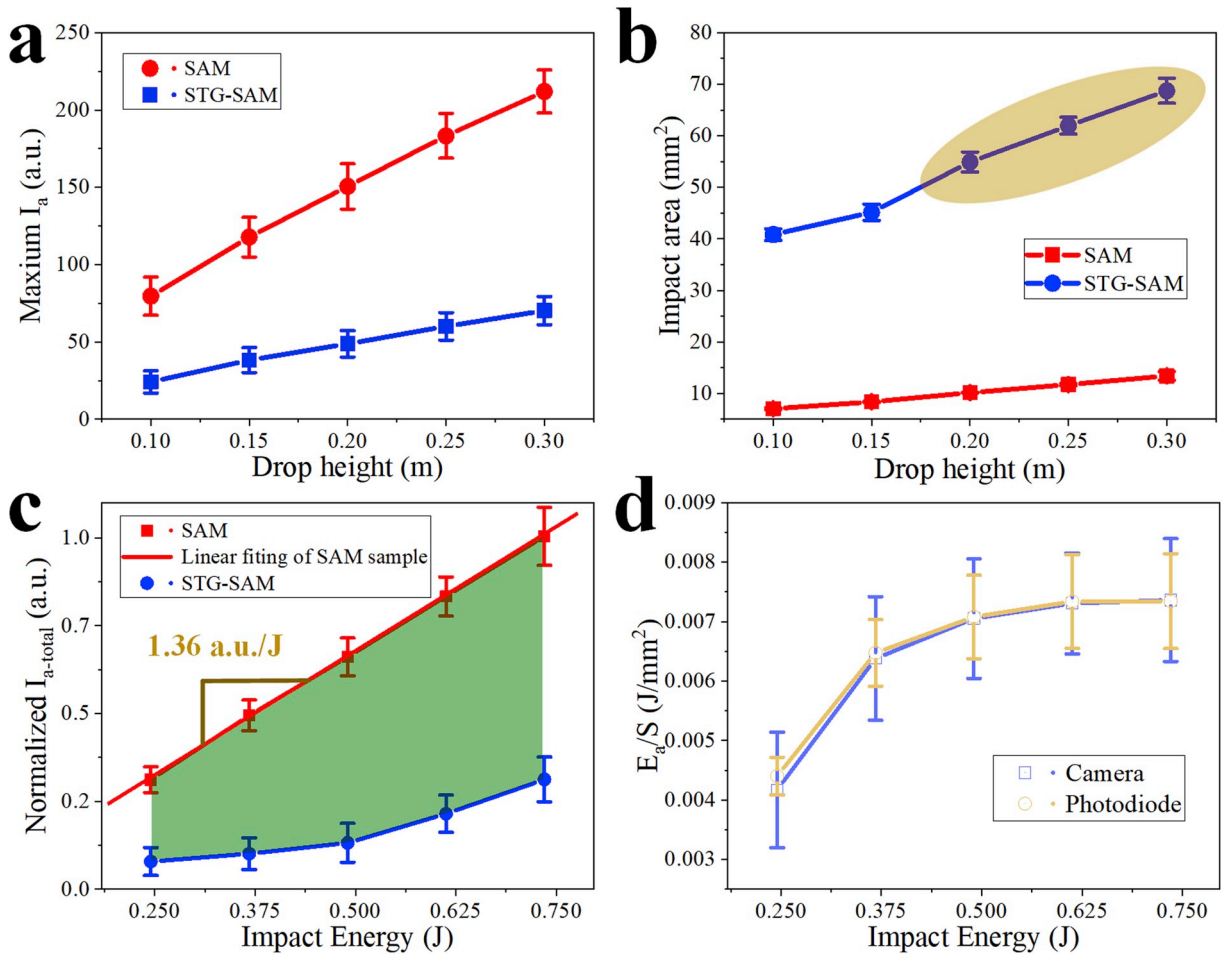

Fig. 6. The maximum I_a (a), impact area (b) versus drop height as the drop hammer pounded on the SAM device and STG-SAM device. The normalized I_a sum (normalized $I_{a\text{-}total}$) against the impact energy (c). The energy absorption unit area-E_a/S versus impact energy and the data was obtained from camera and photodiode, respectively (d).

$$I_{i-total} = \int_0^{t_0} I_{i-r}dt + \int_{t_0}^{\infty} I_{i-d}dt \tag{4}$$

where $I_{i\text{-}total}$ is the time-integration of I_i. For the SAM sample, $I_{i\text{-}total}$ was proportional to the impact energy with a good linearity of 0.998 and a slope of 112 nJ/J, which was consistent with the theory [20]:

$$I_{i-total} \propto E = mgh \tag{5}$$

where E is the total applied energy-the gravitational potential energy (mgh) and m is the mass of drop hammer. As the STG layer was applied, $I_{i\text{-}total}$ was reduced significantly due to the energy absorption behavior of STG. For example, as the drop height was 0.2 m where the impact energy was calculated to be 0.49 J, $I_{i\text{-}total}$ was declined significantly from 54.7 nJ to 11.3 nJ (by 79.3%). The gray zone was the $I_{i\text{-}total}$ reduction owing to energy absorption of STG layer (Fig. S3b). The energy absorption increased with the applied energy, while the increased speed declined gradually.

3.4. Illumination images of SAM and STG-SAM devices under impact

To understand the safeguarding mechanisms of STG under impact, the accumulated illumination images were recorded by using a camera and the spatial I_a distribution was obtained by extracting the gray values of photographs with Matlab 2018b software (Fig. 4). For SAM sample, I_a maps at different drop heights were similar except for the magnitude disparity. Therefore, I_a map at 0.1 m was illustrated here as a typical example (Fig. 4a). Due to the sphere shape of the drop hammer indenter, I_a map exhibited very regular concentric circles with the peak values at the center and zero at the edge. The maximum I_a was 80, and the highest 1/8 I_a (central red part in Fig. 4a) accounted for nearly 35% impact area. In addition, the diameter of the impact region was about 3.1 mm. As the STG layer was applied, the I_a map also demonstrated similar regular concentric circles (Fig. 4b). While the circles distribution was more uniform and the peak I_a was reduced to 24. The diameter of the impact area expanded significantly to almost 7.1 mm. According to equation (5), I_a map presented the energy distribution directly, thus the impressive enlargement of impact area directly induced the declined energy density and reduced I_a. As the drop height increased to 0.2 m (Fig. 4c), the illumination was declined severely at the center while was not influenced at the edge, leading to an obvious I_a platform. Lifting the drop height to 0.3 m, a clear I_a valley was observered at the left part (Fig. 4d). The highest 1/8 I_a (central red part) in the illumination image only accounted for a very small proportion (~12%) of the impact area. Additionally, the diameter of the impact area enlarged from 7.1 mm to 8.3 mm and 9.3 mm with the drop height.

To clarify the rate-dependent mechanical property and phase change induced energy absorption more clearly, the radial relative I_a distribution, illumination images and corresponding STG photographs after impact were illustrated in Fig. 5. In the horizontal axis, a is the impact zone radius and r is the local radius. As the drop hammer pounded on the SAM device directly from 0.1 m (Fig. 5a), the relative I_a was the maximum at the center ($r/a = 0$) and decreased symmetrically to zero at the edge ($r/a = \pm 1$). According to the Hertz contact model [44], as an

elastic sphere impacts on an elastic plate, the pressure distribution is:

$$p(r) = p_0\left(1 - r^2/a^2\right)^{0.5} \tag{6}$$

where $p(r)$ is the pressure at local radius r and p_0 is the maximum pressure at $r/a = 0$. Therefore, the impact energy density distribution ($E(r)$) was related to the local radius r by:

$$E(r) = \frac{p(r)^2}{2Y} = p_0{}^2\left(1 - r^2/a^2\right) \Big/ 2Y \tag{7}$$

where $E(r)$ is the impact energy density at local radius r and Y is Young's modulus of ZnS:Mn layer. According to equations (5) and (7), the relative I_a at local radius r was also proportional to $(1 - r^2/a^2)$. Moreover, the theory (red line) fitted the experiment raw data (blue dots) well. The illumination image captured by camera (Fig. 5a inset) was also approximately centrosymmetric and exhibited strong orange mechanoluminescence.

As the STG protective layer was equipped, the relative I_a behaved similar trend at 0.1 m drop height (Fig. 5b). Differently, the decreasing tendency was not in a quadratic manner. As the SAM device was covered with STG layer, which acted as a Winkle foundation [44], the contact pressure distribution was:

$$p(r) = p_0^{'}\left(1 - r^2/a^2\right) \tag{8}$$

where $p_0^{'}$ is the maximum pressure at $r/a = 0$. Using (5) and (8), the I_a distribution was:

$$I_a(r) \propto E(r) = \frac{p(r)^2}{2Y} = p_0^{'2}\left(1 - r^2/a^2\right)^2 \Big/ 2Y \tag{9}$$

Notably, the theory curve also fitted well with the raw data. As the upper right inset photograph of STG layer depicted, the incompressible STG flowed out of the central loading region and bulged upwards, forming a sphere indentation fitting the shape of drop hammer. Besides, the weak illumination image (middle inset in Fig. 5b) proved that the applied impact energy was largely absorbed and spread by the viscoelastic deformation of STG.

As the drop height increased to 0.2 m (Fig. 5c), the raw data fitted well with the theory at the edge of the impact zone ($|r/a|>0.4$). However, I_a decreased slightly at the central region, leading to the peak loss phenomenon (light blue area in Fig. 5c). In the image of STG layer (upper right inset in Fig. 5c), besides the viscoelastic smooth deformation at the edge, obvious unsmooth area was observed at the central region. This was mainly attributed to the phase change of STG from viscous liquid state to rubbery state and occurrence of microcracks at high strain rate. A corresponding dark zone also appeared in the illumination image. Therefore, the peak loss in the illumination image provided visual and solid proof for energy absorption by phase change. Additionally, this human-readable output confirmed the user-interactive superiority of the mechanoluminescence method.

Increasing the drop height to 0.3 m, the theory only agreed with the raw data at the brink ($|r/a|>0.9$) and at the most central region, the raw data was much lower (Fig. 5d). The peak loss, shown in the light blue area, also enlarged significantly. Notably, a low platform occurred in the left part, which corresponded to the dark valley in Fig. 4d and the inset illumination image (brown circles in Fig. 5d). As the photograph of STG layer depicted, the area of phase change and microcracks expanded dramatically and accounted for most impact zone. A large crack appeared in the left part, which dissipated additional impact energy and resulted in the dark valley of the illumination image. In summary, by relating the illumination I_a distribution to the energy maps, the direct energy absorption of STG under impact was visualized and the underlying physical bases were discovered. Moreover, this example convincingly demonstrated the unique on-site advantage of mechanoluminescence method in the energy visualization for complicated real samples, which provided more physical details than theory.

As the local I_a was related to the local stress directly according to equation (9), the maximum gray values were extracted to evaluate the force dissipation performance of STG under impact (Fig. 6a). As the drop height increased from 0.1 m to 0.2 m, the maximum I_a increased notably from 79.6 to 150 owing to the growing impact energy. STG layer declined the maximum I_a apparently from 150 to 48.8 at 0.2 m drop height, indicating the impact energy was dissipated forcefully by STG. Besides, the increased speed of maximum I_a with the drop height was impeded severely by STG, demonstrating its outstanding energy dissipation performance.

The enlargement of impact area was also essential for the energy and force dissipation, which was an important factor for the safeguarding behavior of STG (Fig. 6b). The rose of drop height expanded the impact area slightly. Notably, as the STG layer was introduced, the impact area almost enlarged 5 times from 7.06 mm^2 to 41.3 mm^2 at 0.1 m drop

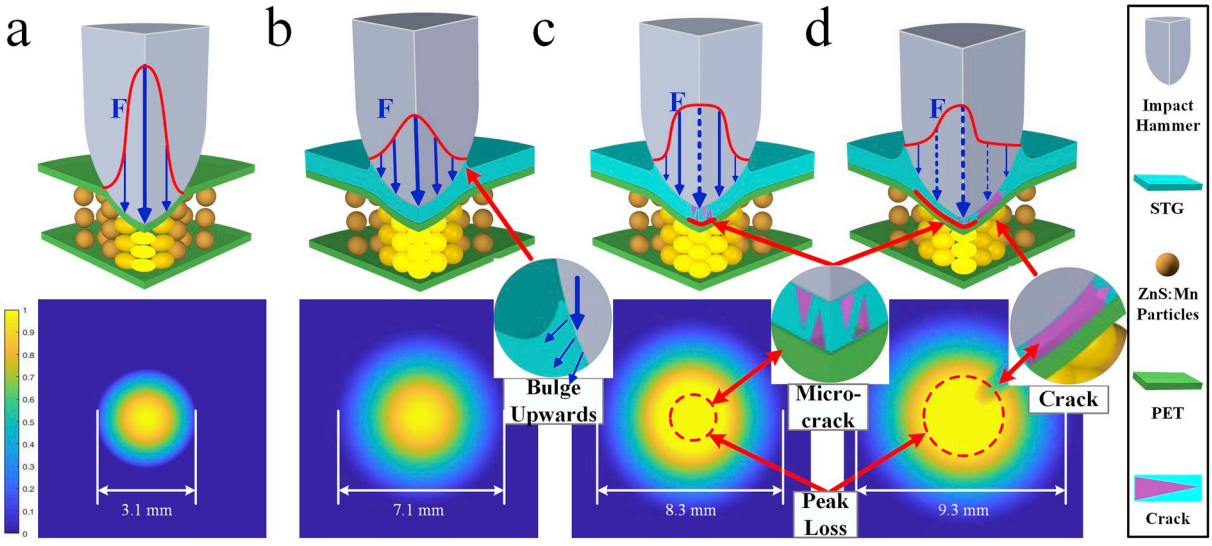

Fig. 7. The schematic diagram of the safeguarding mechanisms of STG layer, involving force (upper, blue arrows) and normalized I_a maps (below). The drop hammer pounded on the SAM device directly from 0.1 m (a). The drop hammer pounded on STG-SAM device from 0.1 m (b), 0.2 m (c) and 0.3 m (d). The inset pictures were enlargement of local physical changes of STG layer. (For interpretation of the references to color in this figure legend, the reader is referred to the Web version of this article.)

height. The enlargement of impact area was mainly attributed to the viscoelastic deformation of STG, which flowed out the central loading region and formed an indentation fitting the shape of drop hammer. More importantly, STG at the surrounding area became tough and carried impact force due to the unique shear thickening property. This marked expanding of impact zone decreased the applied force effectively by 24.9% and declined the impact energy density significantly. Interestingly, the impact area increment also enlarged as drop height exceeded 0.2 m (brown ellipse in Fig. 6b). As STG transformed from viscous liquid state to rubbery state, the occurrence of the second force peak prolonged the buffer time. Thus, the indentation depth of the drop hammer into STG layer was enlarged, which further expanded the impact area. Moreover, the accelerated increase of impact area declined the impact stress and energy density, demonstrating the superior safeguarding performance of STG at high strain rate.

To demonstrate the energy absorption of STG layer, the normalized total I_a ($I_{a\text{-}total}$) was extracted from illumination images (Fig. 6c), corresponding to $I_{i\text{-}total}$ calculated from photodiode data. As the drop hammer pounded on the SAM device directly, the normalized $I_{a\text{-}total}$ was proportional to the impact energy, which matched equation (5) well with a linearity of 0.997 and a slope of 1.36 a.u./J. For example, as the impact energy rose from 0.245 J to 0.735 J, the normalized $I_{a\text{-}total}$ increased from 0.34 to 1.00. As the STG protective layer was equipped, the normalized $I_{a\text{-}total}$ decreased apparently from 0.34 to 0.079 (by 76.8%) at 0.1 m drop height. The green area between the two curves was the normalized $I_{a\text{-}total}$ reduction induced by the energy absorption of STG (Fig. S4). Increasing the impact energy, the energy absorption increased while the increased speed reduced gradually. As impact energy increased from 0.245 J to 0.490 J, the energy absorption expanded quickly from 0.171 J to 0.387 J with an increment of 0.217 J. Further increasing the impact energy to 0.735 J, the energy absorption increment reduced to 0.119 J.

The energy absorption unit area (E_a/S) was also an important factor to evaluate the safeguarding performance of STG (Fig. 6d). E_a/S at first increased gradually to saturation and then kept constant. As the impact energy was 0.245 J, E_a/S was 4.17×10^{-3} J/mm^2. As the impact energy rose to 0.490 J, E_a/S reached 7.07×10^{-3} J/mm^2 owing to the enlarged viscoelastic deformation and the occurrence of phase change. Because of the saturation of phase change area, E_a/S kept about 7.33×10^{-3} J/mm^2 as the drop height exceeded 0.25 m. The results obtained from photodiode exhibited a higher accuracy with smaller data errors. Besides, the acceptable data errors of the above tests also confirmed the high sensitivity and reliability of the mechanoluminescence method.

3.5. The safeguarding mechanisms of STG at low and high strain rate

To clarify the mechanism of safeguarding characteristic of STG under impact clearly, the detailed schematic diagrams (1/4 section view) are demonstrated in Fig. 7. As the drop hammer pounds on the SAM device directly from 0.1 m (Fig. 7a), the upper PET layer endures large and concentrated concave deformation at the impact center. Simultaneously, the ZnS:Mn particles between the PET layers deform severely and illuminate strong orange light. Away from the impact center, the deformation and illumination decrease sharply to zero. In this case, the applied force and energy are concentrated at the loading center, leading to the intensive illumination image.

As the drop hammer impacts upon STG-SAM device from 0.1 m, the incompressible STG flows out the loading center and bulges upwards (Fig. 7b and local enlargement), forming a bowl fitting the sphere shape of impact indenter. At the surrounding area, STG transforms into solid state due to the shear thickening property and carries partial impact force, which expanded impact area forcefully by 5 times with the diameter of impact area increasing incredibly from 3.1 mm to 7.1 mm. Besides, the viscoelastic deformation of STG absorbs impact energy effectively by almost 76.8%. Consequently, more ZnS:Mn particles are compressed while the mechanoluminescence intensity is much weaker. As the drop height increases to 0.2 m, microcracks accompanied by phase change (Fig. 7c and local enlargement) occur in STG at the central loading region. Due to the force/energy absorption of the phase change, the central force/energy density reduces dramatically, inducing the peak loss phenomenon. Besides, the diameter of impact region enlarged from 7.1 mm to 8.3 mm. As the drop height rises to 0.3 m (Fig. 7d), the area of phase change and microcracks expands notably and almost occupies all the impact zone, leading to the enlargement of loss peak area. Furthermore, thanks to the join of surrounding microcracks, a large visible crack is formed, which declines local stress noticeably. Due to the outstanding energy absorption behavior of the large crack, the local illumination is weakened remarkably.

4. Conclusion

In conclusion, a full-field, simple-setup and user-interactive mechanoluminescence method is successfully developed to visualize the force/energy absorption of STG and promote the understanding of safeguarding mechanisms. The double peaks in force and instantaneous intensity signals provide direct proof for force/energy absorption by phase change. Furthermore, by converting the illumination images to energy maps, the visualization of energy absorption is achieved and the underlying physical bases of safeguarding behavior are studied. At low strain rate, the unique shear thickening property and viscoelastic deformation expand impact area by 5 times and buffer impact force by 24.9%, providing reliable safeguarding performance. At high strain rate, the phase change of STG and accompanied cracks absorb extra energy and further increase the impact area. Therefore, this mechanoluminescence-based method paves a way for the academic research and practical applications of ST materials. More inspiringly, this system enables the sensed pressure/energy profile to be visible and detectable without the need for sophisticated data acquisition circuits and electronic boards, which may find a wide range of applications in automotive control panels, interactive input devices, robotics, and medical and health monitoring devices.

Declaration of competing interest

We declare there are no conflicts of interest associated with this work.

Acknowledgments

Financial supports from the National Natural Science Foundation of China (Grant No. 11822209, 11802303, 11772320), the Strategic Priority Research Program of the Chinese Academy of Sciences (Grant No. XDB22040502), the Fundamental Research Funds for the Central Universities (WK2090050045), and the Opening Project of Applied Mechanics and Structure Safety Key Laboratory of Sichuan Province (SZDKF-1701) are gratefully acknowledged. This study was also supported by the Collaborative Innovation Center of Suzhou Nano Science and Technology.

Appendix A. Supplementary data

Supplementary data related to this article can be found at https://doi.org/10.1016/j.compositesb.2019.107564.

References

[1] Brown E, Jaeger HM. Shear thickening in concentrated suspensions: phenomenology, mechanisms and relations to jamming. Rep Prog Phys 2014;77(4):046602.
[2] Mari R, Seto R, Morris JF, Denn MM. Shear thickening, frictionless and frictional rheologies in non-Brownian suspensions. J Rheol 2014;58(6):1693–724.
[3] Gurgen S, Kushan MC, Li WH. Shear thickening fluids in protective applications: a review. Prog Polym Sci 2017;75:48–72.

[4] Obradovic V, Stojanovic DB, Jokic B, Zrilic M, Radojevic V, Uskokovic PS, et al. Nanomechanical and anti-stabbing properties of Kolon fabric composites reinforced with hybrid nanoparticles. Composites, Part B 2017;108:143–52.
[5] Cai ZB, Li ZY, Ding Y, Zheng J, Liu JH, Zhou ZR. Preparation and impact resistance performance of bionic sandwich structure inspired from beetle forewing. Composites, Part B 2019;161:490–501.
[6] Tan Z, Li W, Huang W. The effect of graphene on the yarn pull-out force and ballistic performance of Kevlar fabrics impregnated with shear thickening fluids. Smart Mater Struct 2018;27(7):075048.
[7] Khodadadi A, Liaghat G, Vahid S, Sabet AR, Hadavinia H. Ballistic performance of Kevlar fabric impregnated with nanosilica/PEG shear thickening fluid. Composites, Part B 2019;162:643–52.
[8] Liu KW, Cheng CF, Zhou LY, Zou F, Liang WF, Wang MY, et al. A shear thickening fluid based impact resistant electrolyte for safe Li-ion batteries. J Power Sources 2019;423:297–304.
[9] Fu KK, Wang HJ, Chang L, Foley M, Friedrich K, Ye L. Low-velocity impact behaviour of a shear thickening fluid (STF) and STF-filled sandwich composite panels. Compos Sci Technol 2018;165:74–83.
[10] Zhang X, Zhang H, Wang P, Chen Q, Li X, Zhou Y, et al. Optimization of shear thickening fluid encapsulation technique and dynamic response of encapsulated capsules and polymeric composite. Compos Sci Technol 2019;170:165–73.
[11] Zhang H, Zhang X, Chen Q, Li X, Wang P, Yang E-H, et al. Encapsulation of shear thickening fluid as an easy-to-apply impact-resistant material. J Mater Chem 2017; 5(43):22472–9.
[12] Boland CS, Khan U, Ryan G, Barwich S, Charifou R, Harvey A, et al. Sensitive electromechanical sensors using viscoelastic graphene-polymer nanocomposites. Science 2016;354(6317):1257–60.
[13] Wang YP, Wang S, Xu CH, Xuan SH, Jiang WQ, Gong XL. Dynamic behavior of magnetically responsive shear-stiffening gel under high strain rate. Compos Sci Technol 2016;127:169–76.
[14] Wang S, Ding L, Fan XW, Jiang WQ, Gong XL. A liquid metal-based triboelectric nanogenerator as stretchable electronics for safeguarding and self-powered mechanosensing. Nano Energy 2018;53:863–70.
[15] Han E, Peters IR, Jaeger HM. High-speed ultrasound imaging in dense suspensions reveals impact-activated solidification due to dynamic shear jamming. Nat Commun 2016;7:12243.
[16] Feng A, Smet PF. A review of mechanoluminescence in inorganic solids: compounds, mechanisms, models and applications. Materials 2018;11(4):484.
[17] Zhang H, Wei Y, Huang X, Huang W. Recent development of elastico-mechanoluminescent phosphors. J Lumin 2019;207:137–48.
[18] Yang J, Qin J, Geng P, Wang J, Fang M, Li Z. Molecular conformation-dependent mechanoluminescence: same mechanical stimulus but different emissive color over time. Angew Chem Int Ed 2018;57(43):14174–8.
[19] Zhou H, Du YD, Wu C, Jiang YJ, Wang F, Zhang JC, et al. Understanding the mechanoluminescent mechanisms of manganese doped zinc sulfide based on load effects. J Lumin 2018;203:683–8.
[20] Chandra B, Goutam R, Chandra V, Patel R, Luka A, Baghel R. Luminescence induced by elastic and plastic deformation of II–VI semiconductors at fixed strain rates. Optoelectron Adv Mater Rapid Commun 2009;3(11):1181–9.
[21] Jeong SM, Song S, Joo KI, Kim J, Hwang SH, Jeong J, et al. Bright, wind-driven white mechanoluminescence from zinc sulphide microparticles embedded in a polydimethylsiloxane elastomer. Energy Environ Sci 2014;7(10):3338–46.
[22] Qian X, Cai Z, Su M, Li F, Fang W, Li Y, et al. Printable skin-driven mechanoluminescence devices via nanodoped matrix modification. Adv Mater 2018;30(25):1800291.
[23] Tian X, Lee PM, Tan YJ, Wu TL, Yao H, Zhang M, et al. Wireless body sensor networks based on metamaterial textiles. Nat Electron 2019;2(6):243–51.
[24] Chandra BP, Xu CN, Yamada H, Zheng XG. Luminescence induced by elastic deformation of ZnS:Mn nanoparticles. J Lumin 2010;130(3):442–50.
[25] Chandra BP, Chandra VK, Jha P. Microscopic theory of elastico-mechanoluminescent smart materials. Appl Phys Lett 2014;104(3):031102.
[26] Wu C, Zeng SS, Wang ZF, Wang F, Zhou H, Zhang JC, et al. Efficient mechanoluminescent elastomers for dual-responsive anticounterfeiting device and stretching/strain sensor with multimode sensibility. Adv Funct Mater 2018;28(34): 1803168.
[27] Wang X, Que M, Chen M, Han X, Li X, Pan C, et al. Full dynamic-range pressure sensor matrix based on optical and electrical dual-mode sensing. Adv Mater 2017; 29(15):1605817.
[28] Wang XD, Peng DF, Huang BL, Pan CF, Wang ZL. Piezophotonic effect based on mechanoluminescent materials for advanced flexible optoelectronic applications. Nano Energy 2019;55:389–400.
[29] Moon Jeong S, Song S, Lee S-K, Choi B. Mechanically driven light-generator with high durability. Appl Phys Lett 2013;102(5):051110.
[30] Chandra BP, Chandra VK, Jha P. Piezoelectrically-induced trap-depth reduction model of elastico-mechanoluminescent materials. Physica B 2015;461:38–48.
[31] Wang X, Zhang H, Yu R, Dong L, Peng D, Zhang A, et al. Dynamic pressure mapping of personalized handwriting by a flexible sensor matrix based on the mechanoluminescence process. Adv Mater 2015;27(14):2324–31.
[32] Kersemans M, Smet PF, Lammens N, Degrieck J, Van Paepegem W. Fast reconstruction of a bounded ultrasonic beam using acoustically induced piezo-luminescence. Appl Phys Lett 2015;107(23):234102.
[33] Wang Y, Ding L, Zhao C, Wang S, Xuan S, Jiang H, et al. A novel magnetorheological shear-stiffening elastomer with self-healing ability. Compos Sci Technol 2018;168:303–11.
[34] Wang Y, Gong X, Xuan S. Study of low-velocity impact response of sandwich panels with shear-thickening gel cores. Smart Mater Struct 2018;27(6):065008.
[35] Long R, Mayumi K, Creton C, Narita T, Hui C-Y. Rheology of a dual crosslink self-healing gel: theory and measurement using parallel-plate torsional rheometry. J Rheol 2015;59(3):643–65.
[36] Jiang W, Gong X, Wang S, Chen Q, Zhou H, Jiang W, et al. Strain rate-induced phase transitions in an impact-hardening polymer composite. Appl Phys Lett 2014; 104(12):121915.
[37] Hu T, Xuan S, Ding L, Gong X. Stretchable and magneto-sensitive strain sensor based on silver nanowire-polyurethane sponge enhanced magnetorheological elastomer. Mater Des 2018;156:528–37.
[38] Kim MK, Kim DJ, An YK. Electro-mechanical self-sensing response of ultra-high-performance fiber-reinforced concrete in tension. Composites, Part B 2018;134: 254–64.
[39] Rakotonarivo ST, Payan C, Moysan J, Hochard C. Local damage evaluation of a laminate composite plate using ultrasonic birefringence of shear wave. Composites, Part B 2018;142:287–92.
[40] Park DY, Joe DJ, Kim DH, Park H, Han JH, Jeong CK, et al. Self-powered real-time arterial pulse monitoring using ultrathin epidermal piezoelectric sensors. Adv Mater 2017;29(37):1702308.
[41] Spinelli G, Lamberti P, Tucci V, Vertuccio L, Guadagno L. Experimental and theoretical study on piezoresistive properties of a structural resin reinforced with carbon nanotubes for strain sensing and damage monitoring. Composites, Part B 2018;145:90–9.
[42] Hu S, Shi Z, Zhao W, Wang L, Yang G. Multifunctional piezoelectric elastomer composites for smart biomedical or wearable electronics. Composites, Part B 2019; 160:595–604.
[43] Kou H, Zhang L, Tan Q, Liu G, Lv W, Lu F, et al. Wireless flexible pressure sensor based on micro-patterned Graphene/PDMS composite. Sens Actuators A 2018;277: 150–6.
[44] Barber JR. Contact mechanics. New York: Springer; 2018.